The Astronomical Journal, 150:180 (12pp), 2015 December doi:10.1088/0004-6256/150/6/180

RADIO EMISSION AND ORBITAL MOTION FROM THE CLOSE-ENCOUNTER STAR–BROWN DWARF BINARY WISE J072003.20–084651.2*

Adam J. Burgasser[1], Carl Melis[1], Jacob Todd[2], Christopher R. Gelino[3,4], Gregg Hallinan[4], and Daniella Bardalez Gagliuffi[1]
[1] Center for Astrophysics and Space Science, University of California San Diego, La Jolla, CA 92093, USA; aburgasser@ucsd.edu
[2] Department of Physics and Astronomy, University of California, Los Angeles, CA 90095-1562, USA
[3] NASA Exoplanet Science Institute, Mail Code 100-22, California Institute of Technology, 770 South Wilson Avenue, Pasadena, CA 91125, USA
[4] Infrared Processing and Analysis Center, MC 100-22, California Institute of Technology, Pasadena, CA 91125, USA
Received 2015 July 10; accepted 2015 August 24; published 2015 November 18

ABSTRACT

We report the detection of radio emission and orbital motion from the nearby star–brown dwarf binary WISE J072003.20–084651.2AB. Radio observations across the 4.5–6.5 GHz band with the Very Large Array identify at the position of the system quiescent emission with a flux density of 15 ± 3 μJy, and a highly polarized radio source that underwent a 2–3 minute burst with peak flux density 300 ± 90 μJy. The latter emission is likely a low-level magnetic flare similar to optical flares previously observed for this source. No outbursts were detected in separate narrow-band Hα monitoring observations. We report new high-resolution imaging and spectroscopic observations that confirm the presence of a co-moving T5.5 secondary and provide the first indications of three-dimensional orbital motion. We used these data to revise our estimates for the orbital period ($4.1^{+2.7}_{-1.3}$ year) and tightly constrain the orbital inclination to be nearly edge-on ($93\overset{\circ}{.}6^{+1\overset{\circ}{.}6}_{-1\overset{\circ}{.}4}$), although robust measures of the component and system masses will require further monitoring. The inferred orbital motion does not change the high likelihood that this radio-emitting very low-mass binary made a close pass to the Sun in the past 100 kyr.

Key words: binaries: visual – brown dwarfs – stars: chromospheres – stars: individual (WISE J072003.20–084651.2) – stars: low-mass – stars: magnetic field

1. INTRODUCTION

WISE J072003.20–084651.2 (hereafter WISE J0720–0846) is an M9.5 dwarf originally identified by Scholz (2014) as a possible new member of the local 8 pc sample. It was previously missed in searches for nearby low-mass dwarfs due to its low Galactic latitude ($b = 2\overset{\circ}{.}3$) and small proper motion (121.7 ± 0.3 mas yr^{-1}). Subsequent follow-up observations by Kirkpatrick et al. (2014), Burgasser et al. (2015, hereafter B15), and Ivanov et al. (2015, hereafter I15) confirmed the late-type nature and proximity of the source (6.0 ± 1.0 pc), and have identified it as having an unusually high recessional velocity ($+83.8$ km s^{-1}), indicative of old disk/thick disk kinematics. Mamajek et al. (2015) have deduced that WISE J0720–0846 had one of the closest stellar approaches to the Sun inferred to date, passing within $0.25^{+0.11}_{-0.07}$ pc over a period of 60,000–85,000 years ago, possibly penetrating the outer Oort Cloud.

Evidence for a T-type brown dwarf companion to WISE J0720–0846 was reported by B15, based on both near-infrared spectral analysis and the presence of a candidate resolved source in high-resolution laser guide star adaptive optics (LGSAO) imaging. In support of this, I15 reported infrared excess in 11 and 22 μm photometry from the *Wide-field Infrared Survey Explorer* (*WISE*; Wright et al. 2010) that could be attributed to a low-temperature secondary. However, the detection of the secondary was marginal due to its close separation (140 mas), large magnitude difference with the primary ($\Delta H = 4$), and poor LGSAO correction, and neither B15 nor I15 detected significant radial velocity (RV) variability over overlapping ~3 month timescales. Confirming the presence of this putative companion and assessing the degree of its gravitational perturbation on the primary is important for determining an accurate parallax and space motion for WISE J0720–0846. This system is only the second (candidate) binary to be identified among the 14 known late-M dwarfs within 10 pc of the Sun.

Another remarkable trait of WISE J0720–0846 reported in B15 and I15 is its weak yet highly variable magnetic emission. Quiescent Hα emission was observed to be at or below typical values for M9–L0 dwarfs, with a relative power of $\log_{10} L_{H\alpha}/L_{bol} \approx -5$. However, B15 reported the detection of multiple flaring events, both in white-light photometry and Hα line emission. These flares were infrequent (<1% effective duty cycle) but nevertheless produced order-of-magnitude variations in nonthermal emission. Unfortunately, the X-ray limit of $\log_{10} L_X/L_{bol} \lesssim -3.2$ reported by I15 does not provide a stringent constraint on the high-energy nonthermal emission from this source. Overall, WISE J0720–0846 appears to be similar in magnetic behavior to the rapidly rotating BRI 0021–0040 (Basri & Marcy 1995; Reid et al. 1999), being weakly active but with occasional strong bursts. Deducing how these bursts relate to age or rotation, or in the case of WISE J0720–0846 interaction with a (putative) close companion, may provide critical clues for understanding the overall decline in optical and X-ray magnetic activity across the M dwarf/L dwarf transition (Gizis et al. 2000; Kirkpatrick et al. 2000; West et al. 2004; Stelzer et al. 2006; Schmidt et al. 2014) and contrary trends in nonthermal radio emission (Berger 2006; McLean et al. 2012; Antonova et al. 2013).

In this article, we report new observations of WISE J0720–0846 at optical, near-infrared and radio wavelengths

* Some of the data presented herein were obtained at the W. M. Keck Observatory, which is operated as a scientific partnership among the California Institute of Technology, the University of California and the National Aeronautics and Space Administration. The Observatory was made possible by the generous financial support of the W. M. Keck Foundation.

which confirm both the bursting and binary nature of this source. In Section 2 we report the detection of low-level quiescent and bursting radio emission based on data obtained with the Karl G. Jansky Very Large Array (hereafter VLA), and limits on Hα variability from asynchronous narrow-band photometric monitoring. In Section 3 we report new imaging and high resolution spectroscopic observations that confirm the presence of a T5.5 companion, and provide the first indications of orbital motion. We use these data to make constraints on the orbital configuration of the system in Section 4. Our results are discussed in Section 5.

2. MAGNETIC EMISSION FROM WISE J0720–0846

2.1. Observations

WISE J0720–0846 was observed with the VLA (project code 14B–313, PI Burgasser) in the compact C-configuration (baselines of 0.035–3.4 km) on 2014 November 11 from UT 08:48:50 to 14:47:48. The WIDAR correlator was set up for C-band continuum observations with two basebands, each having eight 128 MHz sub-bands centered at 5.0 and 6.0 GHz, for a frequency range of 4.488–6.512 GHz and a total bandwidth of ≈2 GHz. Each sub-band had four polarization products (RR, LL, RL, LR) and sixty-four 2 MHz channels; a 5 s dump rate was used. After observation of our primary calibration source 3C48 to set the absolute flux scale and measure the complex bandpass, we conducted a sequence of 4 minute cycles, with 3 minutes on WISE J0720–0846 and 1 minute on the gain calibrator QSO J0730–1141. This observational strategy optimizes image quality by frequent monitoring (and hence correction) of phase fluctuations.

All data were reduced with the Astronomical Image Processing Software package (AIPS; Greisen 2003, p. 109) following best practices for wide-band radio data reduction. Radio-frequency interference (RFI) was present throughout the observation, being especially persistent and strong in the sub-bands covering 5.782–6.512 GHz, and also present at varying levels in several other sub-bands. All data affected by RFI were removed. In addition, sub-band 0 of each baseband failed to produce robust data, and these measurements were also removed. After data flagging, our average frequency was 5.27 GHz and our total bandwidth was reduced to ≈1.2 GHz.

2.2. Quiescent Emission

The final cleaned and calibrated data were analyzed by imaging and performing time-series analysis on the *uv*-data. Figure 1 shows imaging of the entire data set (all unflagged times and frequencies) at the coordinates of WISE J0720–0846, which reveals a weak, elongated source. This is interpretted to be a blend between weak quiescent emission from WISE J0720–0846 and an unrelated faint background source, each having similar flux densities of ≈15 μJy.[5] Using the AIPS task DFTPL and the procedures described in Osten & Wolk (2009), we analyzed the time-series data at the peak flux position, shown in Figure 2. This series reveals weak but nonzero emission over the entire course of the observation, with a short burst of emission at UT 13:21:37. Masking out the burst, we measure a mean quiescent flux density of 15 ± 3 μJy with no evidence of statistically significant variability.[6] This is the weakest quiescent emission detected for a very low mass dwarf to date, comparable to the quasi-quiescent emission reported for the T6.5 dwarf 2MASS J10475385 + 2124234 (Williams et al. 2013, 16 ± 5 μJy). The apparent flux density translates into a specific radio luminosity of $\log_{10}L_\nu = (7 \pm 2) \times 10^{11}$ erg s^{-1} Hz^{-1} at the 6.0 ± 1.0 pc distance of WISE J0720–0846, and $\log_{10}\nu_{pk}L_\nu/L_{bol} = -8.49 \pm 0.19$ assuming $\log_{10}L_{bol}/L_\odot = -3.60 \pm 0.05$ (B15; I15) and $\nu_{pk} = 5.28$ GHz. The specific luminosity is 1–2 orders of magnitude below measurements of previously detected late M and L dwarfs (Antonova et al. 2013) and the relative luminosity falls below the activity-rotation relation of McLean et al. (2012) given this source's $v \sin i = 8.6 \pm 0.8$ km s^{-1} (Section 3.4). Indeed, in terms of rotation and radio power, WISE J0720–0846 is similar to the M7 dwarf VB 8 (Krishnamurthi et al. 1999) and the M8 dwarf DENIS J1048–3956 (Burgasser & Putman 2005), both nearby late M dwarfs with weak but variable magnetic emission and modest rotation rates. The weakness of the quiescent emission prevents us from determining either its spectral behavior across the 4.4–6.5 GHz band or its polarization.

2.3. Bursting Emission

A close-up view of the radio burst around UT 13:21 is shown in Figure 2. The burst appears to have begun during observations of the secondary calibrator, so our data sample it only at or after its peak emission. Reimaging of the radio data in the period around this burst shows it to be associated with a bright point source at the coordinates expected for the brown dwarf (Figure 3).[7] The burst is highly polarized, with emission in Stokes *I* of 175 ± 28 μJy and Stokes *V* of –150 ± 28 μJy, implying left-handed circular polarization of 84^{+16}_{-20}% (1σ equivalent uncertainties); i.e., consistent with full polarization. There is no evidence of spectral variation in the burst to within our measurement uncertainties.

We modeled the time series emission as both a rotating spot ("pulse") feature with a Gaussian profile, and as an exponentially declining flare, $f_\nu \propto e^{-t/\tau}$ after peak emission. The former yields a peak flux density of 310 ± 40 μJy, ≈20 times greater than the quiescent emission, and consistent with a total emitted energy of (1.3 ± 0.4) × 10^{24} erg over the 4.5–6.5 GHz band (assuming a flat spectrum). The flare model yields a decay time constant of $\tau = 3.5 \pm 0.9$ minutes and, depending on whether the burst initiated at the start or end of the calibration period, a total emitted energy of (1–3) × 10^{24} erg.

The burst emission occurs for at most 3 minutes during our 5 hr of observation of WISE J0720–0846, or 1% of the total time on-source. This is consistent with the flaring duty cycle inferred from the aperiodic white light bursts reported in B15. Thus, we favor an infrequent flare mechanism for this emission as well. We nevertheless note that the pulse/spot model implies an emission region ≈1°–2° in longitudinal extent (assuming a rotation period of ≈14 hr; see Section 4), which is consistent with previous periodic pulse detections (Hallinan et al. 2007;

[5] A resolved-object fit to this elongated source yields a total integrated flux density of 28 ± 8 μJy; the map rms noise level is 2.8 μJy bm^{-1}.

[6] For 1 minute sampling, we measure $\chi^2 = 296.0$ for 295 degrees of freedom, yielding a *p*-value of 0.46. Note that with the bursting emission included $\chi^2 = 382.5$ and $p < 0.1$%.

[7] The source identified during the flare is free of contamination because the instantaneous sensitivity over the small time range imaged is insufficient to detect the background blend source.

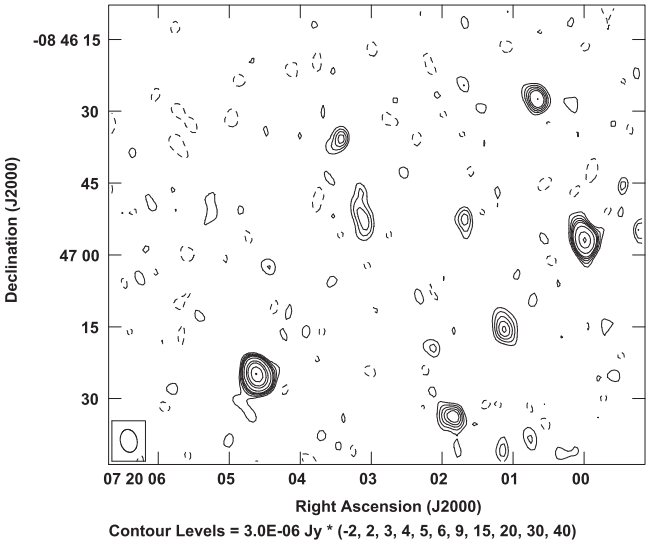

Figure 1. VLA image of the WISE J0720–0846 field integrated over 4.5–6.5 GHz and over the entire time series on 2014 November 14 (UT). Contour levels in flux density are labeled at bottom. The beam shape is indicated in the lower left corner and has dimensions of $4\farcs8 \times 3\farcs5$ with position angle of 11°.5. Emission from WISE J0720–0846 emerges from an extended source spanning $\sim 10''$ along a north–south axis, likely arising from combined emission from the target and an unassociated background source.

Williams & Berger 2015). Longer-term monitoring would be required to distinguish between the flare and pulse hypotheses.

2.4. Hα Monitoring

WISE J0720–0846 was monitored over four nights on 2014 February 18, 20, 22 and 24 (UT) using the facility CCD camera on the 1 m Nickel telescope at Lick Observatory (Table 1). The CCD was configured for 2×2 binning for a pixel scale of $0\farcs37$ pixel^{-1}. After acquisition and centering at *I*-band, WISE J0720–0846 was monitored without dithering through the narrow-band Hα filter ($\lambda_c = 6557$ Å, $\Delta\lambda = 15$ Å), with integration times of 900 s on February 18 and 20 and 300 s on February 22 and 24. Total monitoring periods per night spanned 2.63–3.97 hr, but due to overheads and pauses during occasional clouds the on-source time totalled 7.25 hr over the entire observing run. Bias frames and quartz flat field lamps were also acquired each night for detector calibration.

Data were reduced using standard image reduction techniques. Aperture photometry of WISE J0720–0846 and nearby non-saturated stars was measured using a variable aperture scaled to encapsulate 80% of each source's peak brightness, and an annulus of 63–100 pixels (23″–36″) was used to subtract foreground emission. We did not observe a photometric calibrator during these observations, so no attempt was made to measure absolute Hα fluxes. Instead, we used the mean flux of non-variable stars in the field of view to compute a reference light curve, and used this to normalize the photometry for WISE J0720–0846 over the course of each night. Uncertainties were dominated by source photometry, of order 20%–50%.

We found no significant flux variations over the course of the four nights of observation. At the measured noise level, we can rule out bursts 2–3 times above quiescent emission. B15 reported a single Hα flare with a line flux five times greater than quiescent emission, and an order of magnitude brighter than the local continuum. Such a flare would have been easily

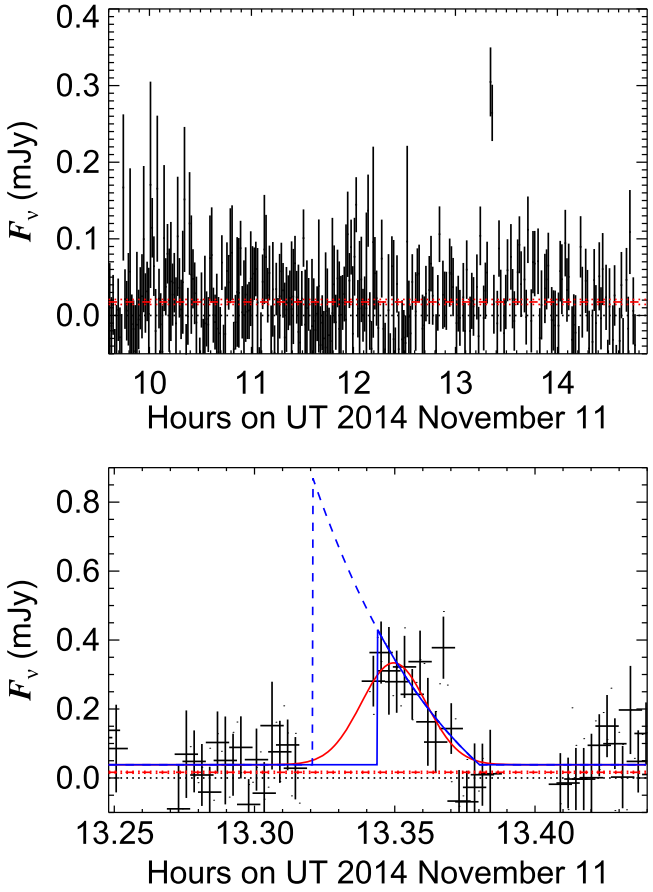

Figure 2. (Top) Time series of radio flux from WISE J0720–0846 in the 4.5–6.5 GHz band with 1 minute sampling; uncertainties are indicated by error bars. The red dashed and dotted lines indicate the mean flux level and 1σ uncertainty, after excluding the bursting emission at UT 13:21. (Bottom) Close-up view of the burst emission, with data sampled every 10 s. Breaks correspond to observations of the secondary calibrator. The best-fit Gaussian (red solid curve) and exponential decay (blue curves: dashed for peak emission at the start of calibration observation, solid for peak emission at the end) models are overplotted.

detected in our observations had it occured. Assuming a flare period of ≈5 minutes, we infer a flare indicidence rate of <1%, similar to the white light flare rates reported in B15 and the radio flare reported here. All of these observations reinforce the conclusion that WISE J0720–0846 is a weakly active and infrequently bursting source.

3. CONFIRMING THE MULTIPLICITY OF WISE J0720–0846

3.1. High Resolution Imaging

WISE J0720–0846 was re-observed with the Near-infraRed Camera 2 (NIRC2) and LGSAO system (van Dam et al. 2006; Wizinowich et al. 2006) on the Keck II 10 m Telescope on 2015 January 11 (UT) in mostly clear and windy conditions with $0\farcs8$ seeing. The narrow field of view (FOV) camera was used to obtain dithered observations in broad-band MKO[8] *J*, *H* and K_s filters, and the medium-band CH_4s filter sampling 1.54–1.65 μm. The $R = 16.8$ mag field star USNO 0812–0137390 was used to correct for tip-tilt aberrations. We

[8] Mauna Kea Observatories near-infrared filter set (Simons & Tokunaga 2002; Tokunaga et al. 2002).

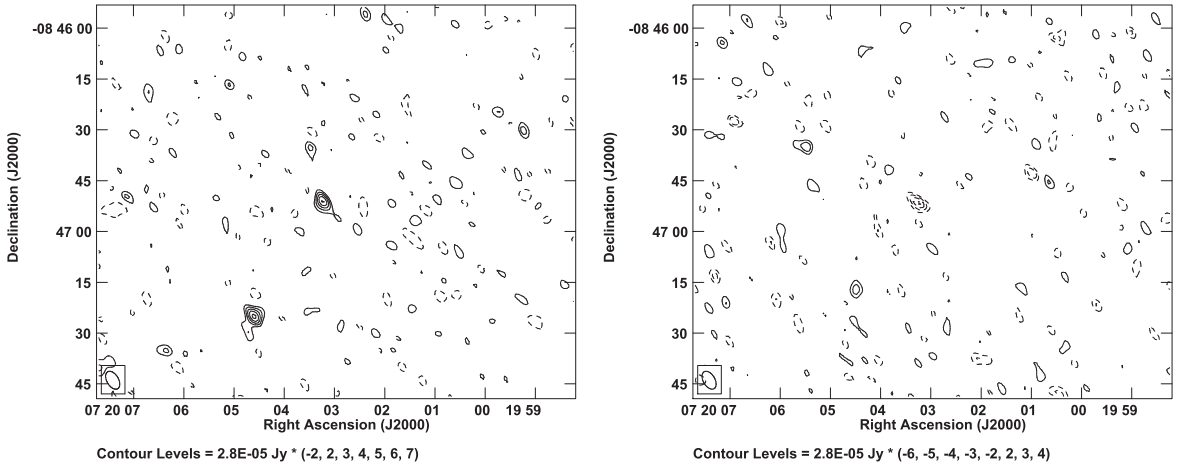

Figure 3. VLA image of the WISE J0720–0846 field in Stokes *I* (left) and *V* (right) integrated over 4.5–6.5 GHz and over the period UT 13:19:07 to 13:24:07. The burst emission seen in the time series data is associated with a point source at the expected position of WISE J0720–0846. The Stokes *V* image shows a negative source of comparable brightness indicating nearly 100% left circular polarization.

Table 1
Hα Monitoring Observations

UT Date	MJD	t_{int} (s)	N_{obs}	UT Start	Duration (hr)	Mean S/N per Measurement
2014 Feb 18	56706.26	900	11	4:42:32	3.03	4
2014 Feb 20	56708.24	900	10	4:38:51	2.63	3
2014 Feb 22	56710.24	300	38	3:55:13	3.97	4
2014 Feb 24	56712.28	300	13	4:55:02	3.52	3

achieved better Strehl ratios than observations reported in B15, 10%–20% depending on wavelength. This allowed us to easily resolve the candidate companion reported in that study in all four filters, as shown in Figure 4.

3.2. Common Proper Motion and Orbital Motion

To extract relative photometry and astrometry, we performed point source function (PSF) fitting of each individual image using a two-dimensional asymmetric Moffat profile optimized to the PSF of the primary component (i.e., with the secondary masked). Measurements are reported in Table 2. We find a separation of 197 ± 3 mas at position angle 256°.7 ± 0°.6, wider than, and at a marginally distinct position angle as, the candidate source previously reported (139 ± 14 mas at 262° ± 2°). As the source detected in these data would have been easily resolved in prior observations, we conclude that statistically significant relative motion has been observed between the two epochs.

Relative motion can be due to differential motion between two physically unrelated sources or orbital motion in a gravitationally bound binary. Figure 5 displays the estimated center of mass motion and component positions between our 2014 and 2015 imaging data, assuming systemic astrometry from B15 and $q = 0.4$ (see below). It is clear that the predominant motion of both sources is co-aligned with the proper motion of the system, particularly in declination; the change in position angle is inconsistent with the secondary being an unmoving background source at the 16σ confidence level. We therefore determine that WISE J0720–0846 is a co-moving binary system, and identify significant astrometric orbital motion over a one year period.

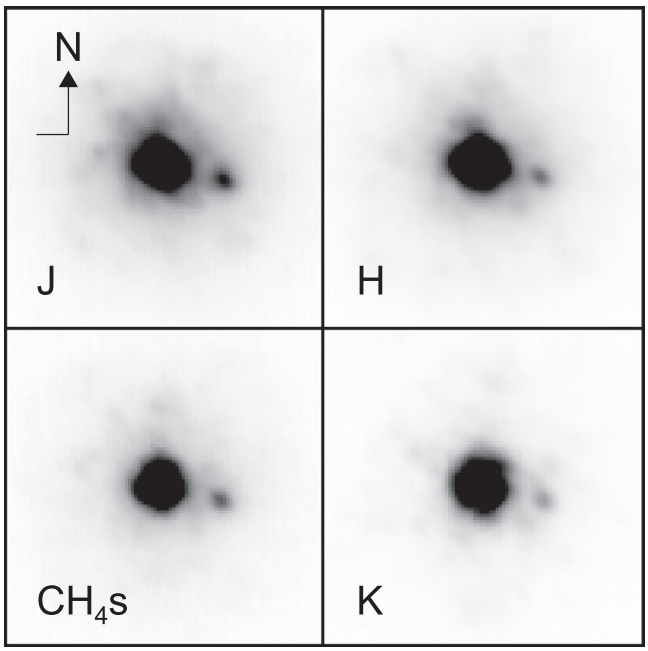

Figure 4. Resolved imaging of the WISE J0720–0846 system with NIRC2/LGSAO. Images are aligned with north up and east to the left, and each box displays an angular scale of 1″. Images are logarithmically flux-scaled to make the faint secondary visible.

3.3. Improved Determination of the Secondary Classification

Our new observations provide greatly improved relative photometry of the two components in the four bands measured, and refine the coarse ΔH estimate from B15 (Table 2). There is a significant difference in relative brightnesses in the CH_4s and

Table 2
Resolved Photometry and Astrometry of WISE J0720–0846

Parameter	Value
ΔJ	2.92 ± 0.07
ΔCH_4s	3.05 ± 0.08
ΔH	3.85 ± 0.11
ΔK_s	4.07 ± 0.20
ρ (mas)	197 ± 3
ρ (AU)	1.19 ± 0.21
PA (°)	256.7 ± 0.6
Primary SpT[a]	M9.5 ± 0.5
Secondary SpT[a]	T5.5 ± 0.5

Note.
[a] Based on spectral template fitting with templates constrained to have the same relative flux scaling as measured in the JHK_s NIRC2 bands.

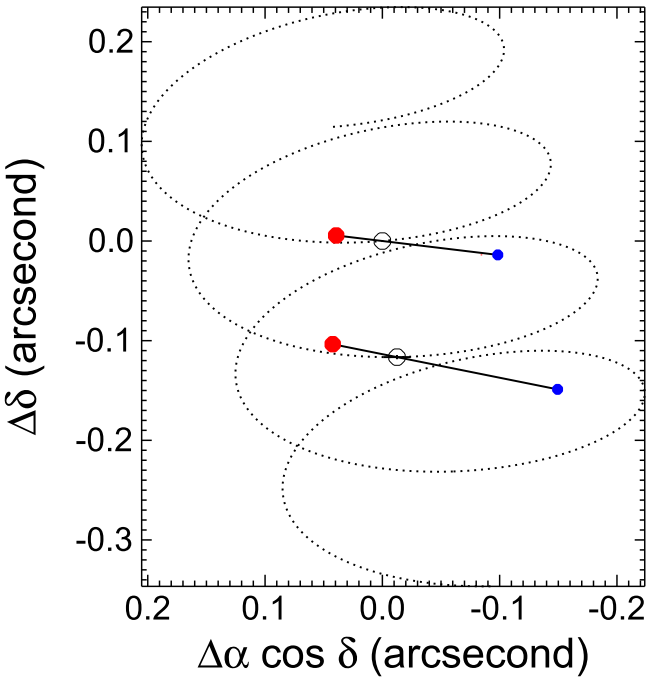

Figure 5. Positions of WISE J0720–0846A (red points) and B (blue points) in our 2014 and 2015 LGSAO images relative to center-of-mass astrometric motion (black points and dotted line) based on values from B15 and assuming $q = 0.4$. The 3σ uncertainties on the center-of-mass position at the 2015 epoch relative to 2014 are indicated: $\sigma_\alpha = 4$ mas, $\sigma_\delta = 0.8$ mas. The relative motion of the two sources is consistent with physical association and orbital motion.

H-band filters consistent with strong CH_4 absorption in the secondary. We used the relative photometry to better constrain the spectral types of the components through spectral template fitting. Following the procedures described in Burgasser et al. (2011), we combined 512 M7-L1 and 125 T0-T7 spectral templates from the SpeX Prism Library (SPL; Burgasser 2014), scaled so that that relative spectrophotometry agreed to within 1σ of the NIRC2 JHK_s measurements.[9] We compared the 16394 binary templates that satisfied these constraints to the combined light SpeX spectra of WISE J0720–0846 from both Kirkpatrick et al. (2014) and B15, following the methods described in the latter paper. Figure 6 shows the best fitting template to the B15 spectrum. Both analyses yield identical results, with component types M9.5 ± 0.5 and T5.5 ± 0.5. The secondary is a half subtype later than, but formally consistent with, the classification reported in B15.

[9] NIRC2 CH_4s photometry was not used for this analysis as the filter profile was unavailable in a digital format (H. Tran 2015, private communication).

3.4. High Resolution Spectroscopy

New high resolution optical and near-infrared spectroscopy of WISE J0720–0846 were obtained with the Near InfraRed Spectrometer (NIRSPEC; McLean et al. 2000) on the Keck II telescope on 2014 December 8 (UT), and with the Hamilton echelle spectrograph (Vogt 1987) on the Lick Observatory Shane 3 m telescope on 2015 March 10 (UT). Data were acquired and reduced as described in B15. The NIRSPEC spectrum (Figure 7) is of high quality (median S/N = 82) and similar to data reported in B15. The Hamilton data had a somewhat lower signal-to-noise ratio (S/N) than prior observations (S/N ≈ 5 at 7500 Å) due to a shorter total integration of 3000 s.

Both spectra were analyzed as described in B15 for radial motion and, for the Hamilton data, Hα emission equivalent width (EW). Despite the low S/N, cross-correlation of the Hamilton spectrum with contemporaneous observations of the RV standard GJ 251 yielded an RV = +86.4 ± 0.5 km s^{-1}, significantly different than the mean motion reported in B15 (+82.5 ± 0.4 km s^{-1}). Marginal Hα emission was observed in these data, with EW = −2 ± 1 Å, consistent with the lowest emission states observed in B15.

For the NIRSPEC data, we re-analyzed the observations reported here and the 2014 observations using an updated Markov Chain Monte Carlo (MCMC) adaptation of the forward-modeling method described in Blake et al. (2010) and B15. We used the BT-Settl atmosphere models (Allard et al. 2012) with updated solar abundance values from Caffau et al. (2011) over an effective temperature ($T_{\rm eff}$) range of 1600–2900 K and surface gravity ($\log g$) range of 4.5–5.5 (cgs). The Solar atlas of Livingston & Wallace (1991) was used to model telluric absorption features. Table 3 summarizes the RV and rotational velocities (v sin i) inferred from these analyses, while Figure 7 shows the best-fit model, with $T_{\rm eff}$ = 2700 K and $\log g$ = 5.5, to the most recent NIRSPEC observations. The rotational velocity measurements are mutually consistent, with a mean value of v sin i = 8.6 ± 0.4 km s^{-1}. However, like the Hamilton observations, the most recent NIRSPEC RV measurement of +85.2 ± 0.2 km s^{-1} is significantly distinct from the mean RV reported in B15 (+83.7 ± 0.4 km s^{-1}) and follows the trend of increasing recessional motion. With these independent measurements, we conclude that WISE J0720–0846A is an RV variable gravitationally perturbed by its brown dwarf secondary.

We note that the best-fitting models for the forward-modeling analyses were consistently in the ranges $T_{\rm eff}$ = 2500–2800 K and $\log g$ = 5.0–5.5. The temperatures are somewhat higher than those expected for an M9.5 dwarf ($T_{\rm eff} \approx 2300$ K; Stephens et al. 2009), but the surface gravity is consistent with the lack of Li I absorption and low-surface gravity spectral features, indicating an age $\gtrsim$1 Gyr. We verified that lower temperature and lower surface gravity models yielded identical RVs, so this measurement appears to be insensitive to the specific model over the parameter range examined here. A robust investigation of the atmospheric parameters of this source is deferred to a later study.

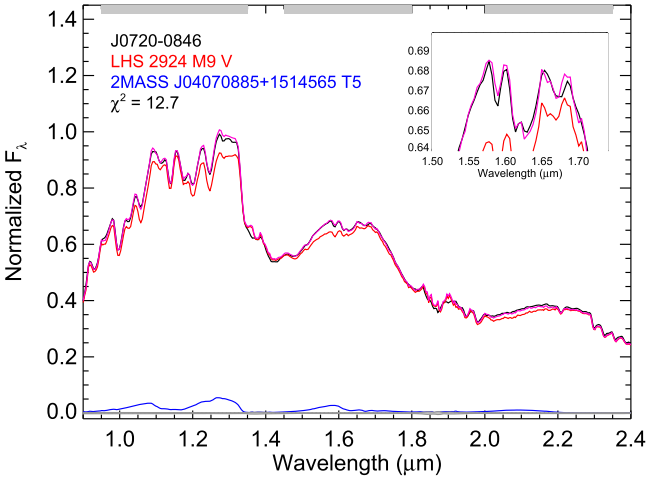

Figure 6. Best-fit spectral binary template (purple line) to the combined-light SpeX spectrum of WISE J0720–0846 (black line) based on scaling spectral templates to the relative JHK_s photometry measured from NIRC2 observations. Best-fit primary (red line; LHS 2924, data from Burgasser & McElwain 2006) and secondary templates (blue line, 2MASS J04070885+1514565, data from Burgasser et al. 2004) are shown at their relative scaling. The gray bars at top indicate the regions over which the fitting was done.

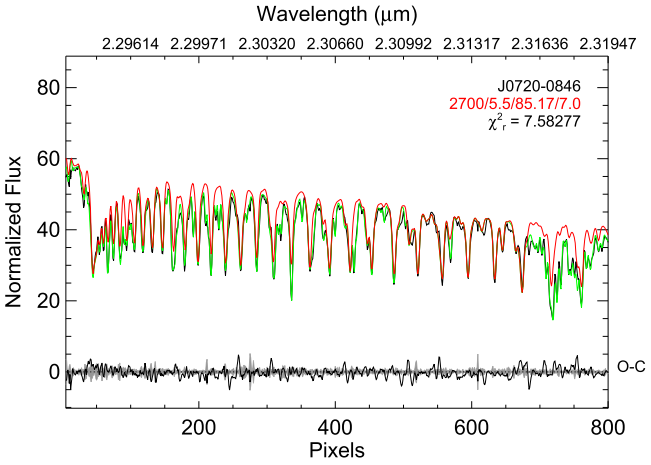

Figure 7. Extracted high-resolution ($\lambda/\Delta\lambda$ = 20,000) K-band spectrum of WISE J0720–0846 obtained with NIRSPEC on UT 2014 December 8 (black line), compared to a best-fit model combining a $T_{\rm eff}$ = 2700 K, log g = 5.5 atmosphere model from Allard et al. (2012, red line) with scaled telluric absorption (green line). The difference between data and model (O–C) is shown in black at the bottom of the plot and is dominated by fringing residuals; the $\pm1\sigma$ uncertainty spectrum is indicated in gray.

Table 3
Radial and Rotational Velocities from NIRSPEC Observations

UT Date	MJD	RV (km s^{-1})	v sin i (km s^{-1})
2014 Jan 19	56676.00968	+84.0 ± 0.3	8.8 ± 0.7
2014 Jan 20	56677.00048	+83.2 ± 0.2	9.3 ± 0.8
2014 Mar 10	56725.71832	+82.9 ± 0.5	6.6 ± 2.3
2014 Apr 12	56758.74056	+84.3 ± 0.4	9.9 ± 1.8
2014 Dec 8	56999.00802	+85.2 ± 0.3	7.6 ± 0.8
Mean	···	+83.8 ± 0.8[a]	8.6 ± 0.8

Note.
[a] χ^2 = 35.9 indicates data inconsistent with a constant radial velocity.

4. IMPROVED CONSTRAINTS ON THE ORBIT OF WISE J0720–0846AB

4.1. Methodology

With WISE J0720–0846AB verified as a gravitationally bound binary with orbital motion detected in all three spatial dimensions, we can begin to constrain the orbital properties of the system and the physical properties of its components. We adapted the MCMC analysis described in Burgasser et al. (2012) to include both RV and relative astrometry measurements. We employed an orbit model with nine parameters,

$$\boldsymbol{\theta} = \left(P, a, e, i, \omega, \Omega, M_0, q, V_{\rm COM}, d\right) \quad (1)$$

where P is the period of the orbit in years, a is the semimajor axis in AU, e is the eccentricity, i is the inclination, ω is the argument of periastron, Ω is the longitude of nodes, M_0 is the mean anomaly at epoch τ_0 = 2014.0896 (MJD[10] = 56675.982), $q \equiv M_2/M_1$ is the system mass ratio, $V_{\rm COM}$ is the center of mass (systemic) RV in km s^{-1}, and d is the distance in pc. The primary RV as a function of time t, $V_1(t)$, is

$$V_1(t) = K_1[e\cos\omega + \cos(T(t)+\omega)] + V_{\rm COM} \quad (2)$$

where

$$K_1 = \frac{2\pi a \sin i}{P\sqrt{1-e^2}}\frac{q}{1+q} \quad (3)$$

and the true anomaly $T(t)$ is related to the eccentric anomaly $E(t)$ through

$$\tan\frac{T(t)}{2} = \sqrt{\frac{1+e}{1-e}}\tan\frac{E(t)}{2} \quad (4)$$

which is solved by Kepler's equation:

$$M(t) - M_0 = 2\pi\frac{t-\tau_0}{P} = E(t) - e\sin E(t). \quad (5)$$

The angular separation vector from primary component to secondary component, $\boldsymbol{\rho} = (\Delta\alpha(t), \Delta\delta(t))$ is determined from

$$\Delta\alpha(t) = \frac{a}{d}\left[A(\cos E(t) - e) + F\sqrt{1-e^2}\sin E(t)\right] \quad (6)$$

$$\Delta\delta(t) = \frac{a}{d}\left[B(\cos E(t) - e) + G\sqrt{1-e^2}\sin E(t)\right] \quad (7)$$

where $\Delta\alpha$ and $\Delta\delta$ are the angular separations on sky measured in arcseconds, and A, B, F and G are the Thiele-Innes constants (Innes 1907; van den Bos 1927):

$$A = \cos\omega\cos\Omega - \sin\omega\sin\Omega\cos i \quad (8)$$

$$B = \cos\omega\sin\Omega + \sin\omega\cos\Omega\cos i \quad (9)$$

$$F = -\sin\omega\cos\Omega - \cos\omega\sin\Omega\cos i \quad (10)$$

$$G = -\sin\omega\sin\Omega + \cos\omega\cos\Omega\cos i. \quad (11)$$

Note that the total system mass ($M_{\rm tot} = a^3/P^2$ in solar masses) and component masses ($M_1 = M_{\rm tot}/[1-q]$, $M_2 = qM_1$) could in principle be uniquely inferred from these parameters if sufficiently constrained.

We selected an initial parameter set that visually coincided with the observations through manual experimentation. We then computed a chain of 10^7 parameter sets using the

[10] Modified Julian Date = Julian Date-2400000.5.

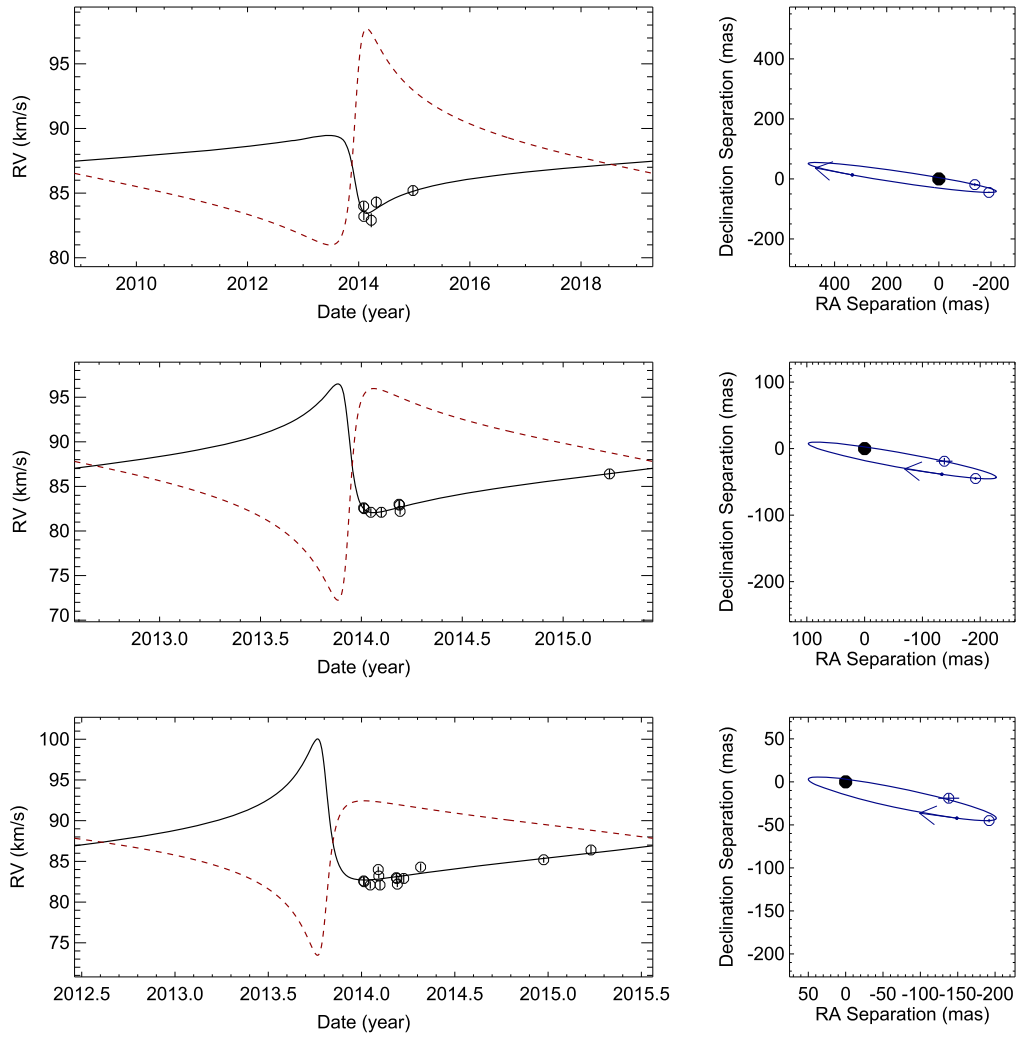

Figure 8. Best-fit orbit from MCMC analysis based on NIRSPEC + NIRC2 data (top), Hamilton Spectrograph + NIRC2 data (middle), and all data (bottom). The left panels show the radial motion of both the primary (solid black line) and secondary (red dashed line) motion compared to primary RV measurements (open circles with error bars). The right panels show the orbital motion of the secondary (blue line) relative to the primary (black dot at the origin) projected on the sky, compared to NIRC2 measurements (open circles; error bars are small on this scale). The arrow indicates the direction of orbital motion at apoapse. Note the different scales for the different fits.

Metropolis–Hastings algorithm (Metropolis et al. 1953; Hastings 1970), at each step varying parameter $\theta_j \rightarrow \theta'_j$ by drawing a random offset from a normal distribution

$$P\left(\theta'_j \middle| \theta_j\right) \propto e^{-\frac{\left(\theta'_j-\theta_j\right)^2}{2\beta_j^2}} \tag{12}$$

where $\boldsymbol{\beta}$ is the set of jump steps.[11] We applied additional parameter constraints of 0.5 year $< P <$ 30 year, $e < 0.8$ and 4 pc $< d <$ 8 pc to eliminate improbable regions of parameter space; note that the eccentricity cutoff is beyond the $e \approx 0.6$ limit suggested in empirical data by Dupuy & Liu (2011). We also limited the component masses to $0.055\,M_\odot < M_1 < 0.15\,M_\odot$ given the spectral classification of the primary and lack of Li I absorption in its optical spectrum (B15; I15), and $M_2 < 0.075 M_\odot$ given the substellar nature of the secondary. Orbit models were compared to the data using a χ^2 statistic that combined both RV and relative astrometric measurements:

$$\chi^2 = \sum_{i=1}^{N_{\rm RV}} \frac{\left({\rm RV}_i^{\rm (obs)} - {\rm RV}_i^{\rm (model)}\right)^2}{\sigma^2_{{\rm RV},i}} + \sum_{j=1}^{N_{\rm ast}} \frac{\left(\Delta\alpha_j^{\rm (obs)} - \Delta\alpha_j^{\rm (model)}\right)^2}{\sigma^2_{\Delta\alpha,j}} + \sum_{j=1}^{N_{\rm ast}} \frac{\left(\Delta\delta_j^{\rm (obs)} - \Delta\delta_j^{\rm (model)}\right)^2}{\sigma^2_{\Delta\delta,j}} \tag{13}$$

where $N_{\rm RV}$ and $N_{\rm ast}$ are the number of RV and astrometric measurements, respectively, and σ the measurement errors. Model values were calculated at the same epochs as the observations. The criterion to adopt successive parameter sets was $U(0, 1) \leqslant e^{-0.5\left(\chi^2_{(j')} - \chi^2_{(j)}\right)}$, where $U(0, 1)$ is a random number drawn from a uniform distribution between 0 and 1. We compared models to data after each individual parameter change rather than changing all parameters, a procedure we

[11] We used in initial set $\boldsymbol{\beta}$ = (3 year, 0.5 AU, 0.2, 10°, 10°, 10°, 10°, 0.2, 1.0 km s^{-1}, 1.0 pc).

Table 4
Parameters from Orbital Analysis

Parameter	NIRSPEC+NIRC2		Hamilton+NIRC2		All Data	
	Best-fit	Median	Best-fit	Median	Best-fit	Median
Modeled Parameters						
Best χ^2	5.83	...	2.84	...	27.6	...
P[a] (year)	10.4	$6.1^{+5.1}_{-2.6}$	2.9	$4.1^{+2.7}_{-1.3}$	3.1	$4.5^{+2.7}_{-1.4}$
a (AU)	2.4	$1.7^{+0.9}_{-0.5}$	1.1	$1.3^{+0.5}_{-0.3}$	1.1	$1.4^{+0.5}_{-0.3}$
e[a]	0.79	$0.72^{+0.06}_{-0.09}$	0.79	$0.77^{+0.02}_{-0.04}$	0.80	$0.76^{+0.03}_{-0.04}$
i (°)	92.1	$94.1^{+2.2}_{-1.7}$	92.8	$93.6^{+1.6}_{-1.4}$	94.9	$94.4^{+1.8}_{-1.6}$
ω (°)	109	83^{+20}_{-24}	70	76^{+17}_{-17}	54	74^{+16}_{-16}
Ω (°)	81.7	$82.2^{+2.3}_{-2.1}$	82.4	$82.7^{+2.1}_{-2.1}$	82.2	$83.3^{+2.2}_{-2.2}$
M_0 (°)	5	20^{+15}_{-11}	10	13^{+8}_{-6}	24	17^{+8}_{-7}
q	0.36	$0.61^{+0.21}_{-0.18}$	0.61	$0.77^{+0.15}_{-0.17}$	0.91	$0.75^{+0.16}_{-0.17}$
V_{COM} (km s^{-1})	87.2	$87.3^{+0.9}_{-0.9}$	87.3	$87.4^{+0.8}_{-0.8}$	87.4	$87.5^{+0.7}_{-0.7}$
d[a] (pc)	4.5	$6.7^{+0.8}_{-1.0}$	4.5	$5.4^{+0.8}_{-0.7}$	6.8	$6.2^{+0.7}_{-0.7}$
Inferred Parameters						
M_{tot} ($M_\odot$)	0.13	$0.13^{+0.04}_{-0.03}$	0.17	$0.15^{+0.03}_{-0.03}$	0.16	$0.15^{+0.03}_{-0.03}$
M_1($M_\odot$)	0.098	$0.080^{+0.032}_{-0.018}$	0.105	$0.082^{+0.026}_{-0.015}$	0.081	$0.081^{+0.028}_{-0.016}$
M_2 ($M_\odot$)	0.035	$0.051^{+0.013}_{-0.014}$	0.064	$0.064^{+0.008}_{-0.010}$	0.074	$0.062^{+0.009}_{-0.011}$
K_1 (km s^{-1})	3.0	$4.4^{+1.2}_{-1.0}$	7.2	$6.3^{+1.1}_{-1.0}$	8.7	$6.0^{+1.1}_{-0.8}$
K_2 (km s^{-1})	8.4	$7.3^{+2.2}_{-1.6}$	11.9	$8.5^{+2.1}_{-1.6}$	9.5	$8.2^{+2.1}_{-1.6}$

Note.
[a] Parameter was constrained to a limited value range in MCMC analysis.

found greatly improved the acceptance rate, which declined from 10% to 1% through the chain. Separate fits were made to the NIRSPEC + NIRC2 and Hamilton + NIRC2 measurements, and to all of the data. Note that in the last case we did not take into account a possible velocity offset between the RV datasets (Ford 2005).

To test for convergence, we monitored parameter autocorrelation and the evolution of subchain variance through the chain. We also generated $M = 10$ chains of length $2n = 10^6$ steps on the Hamilton + NIRC2 data, varying the initial parameter set $\boldsymbol{\theta}_{\rm init}$ as

$$\boldsymbol{\theta}_{\rm init} = \boldsymbol{\theta}_p + N(0, 1)\boldsymbol{\sigma}_p \quad (14)$$

where $\boldsymbol{\theta}_p$ and $\boldsymbol{\sigma}_p$ are the median and half quantile ranges of the posterior parameter distributions (see below) and $N(0, 1)$ is a normal distribution centered on zero with unit variance. We quantified the within chain and between chain variance of all parameters using the Gelman & Rubin (1992) scale reduction factor

$$R_k^2 = 1 + \frac{1}{n}\left(\frac{B_k}{W_k} - 1\right) \quad (15)$$

where $W_k = \bar{\xi}_k$ is the within chain variance for parameter θ_k, equal to the average of parameter variances $\xi_{jk} = \frac{1}{n-1}\sum_{i=1}^{n}(\theta_{ijk} - \bar{\theta}_{jk})^2$ for each of the ten chains using the second half of the chains as the sample; and $B_k = \frac{n}{M-1}\sum_{j=1}^{M}(\bar{\theta}_{jk} - \bar{\bar{\theta}}_k)^2$ is the between chain variance, equal to the variance in parameter averages $\bar{\theta}_{jk}$. Scale reduction factors were within 5% of unity for all modeled parameters with the exception of P (1.35), a (1.37) and ω (1.51). As described below, these three parameters were weakly constrained, and this analysis suggests that the primary MCMC chains may not converge for our limited datasets, reemphasizing that the orbital results presented here should be considered preliminary.

4.2. Results

Figure 8 shows the best-fit orbits from our separate analyses of the RV and imaging datasets. Table 4 lists the best-fit orbital and component parameters, as well as the median and 16% and 84% quantiles of the parameter distributions, after eliminating the first 10% of each chain. Figures 9 through 11 display the distributions and correlations of parameters P, a, e, i, q and M_{tot} for all three datasets.

The best-fit orbits are exceptionally good fits for the individual RV datasets, with $\chi^2 = 5.83$ for nine data points (zero degrees of freedom) for NIRSPEC + NIRC2 and $\chi^2 = 2.84$ for twelve data points (three degrees of freedom) for Hamilton + NIRC2. Note that these low χ^2 values largely reflect the underconstained nature of the solution in orbital phase; i.e., a relatively large family of solutions is formally consistent with these data. The combined dataset yields a somewhat poorer best fit, with modest disagreement between contemporary NIRSPEC and Hamilton RVs driving the χ^2 values. Nevertheless, this solution is nearly identical to that of the Hamilton + NIRC2 dataset. While the best-fit solutions between the NIRSPEC + NIRC2 and the Hamilton + NIRC2 datasets are distinct, the median parameters are consistent within the uncertainties for all datasets. Since parameters inferred from the Hamilton + NIRC2 data are best constrained, we refer to these in the following discussion.

Several of the parameters are very well constrained, most notably the orbital inclination ($i = 93.^\circ6^{+1.^\circ6}_{-1.^\circ4}$), the longitude of

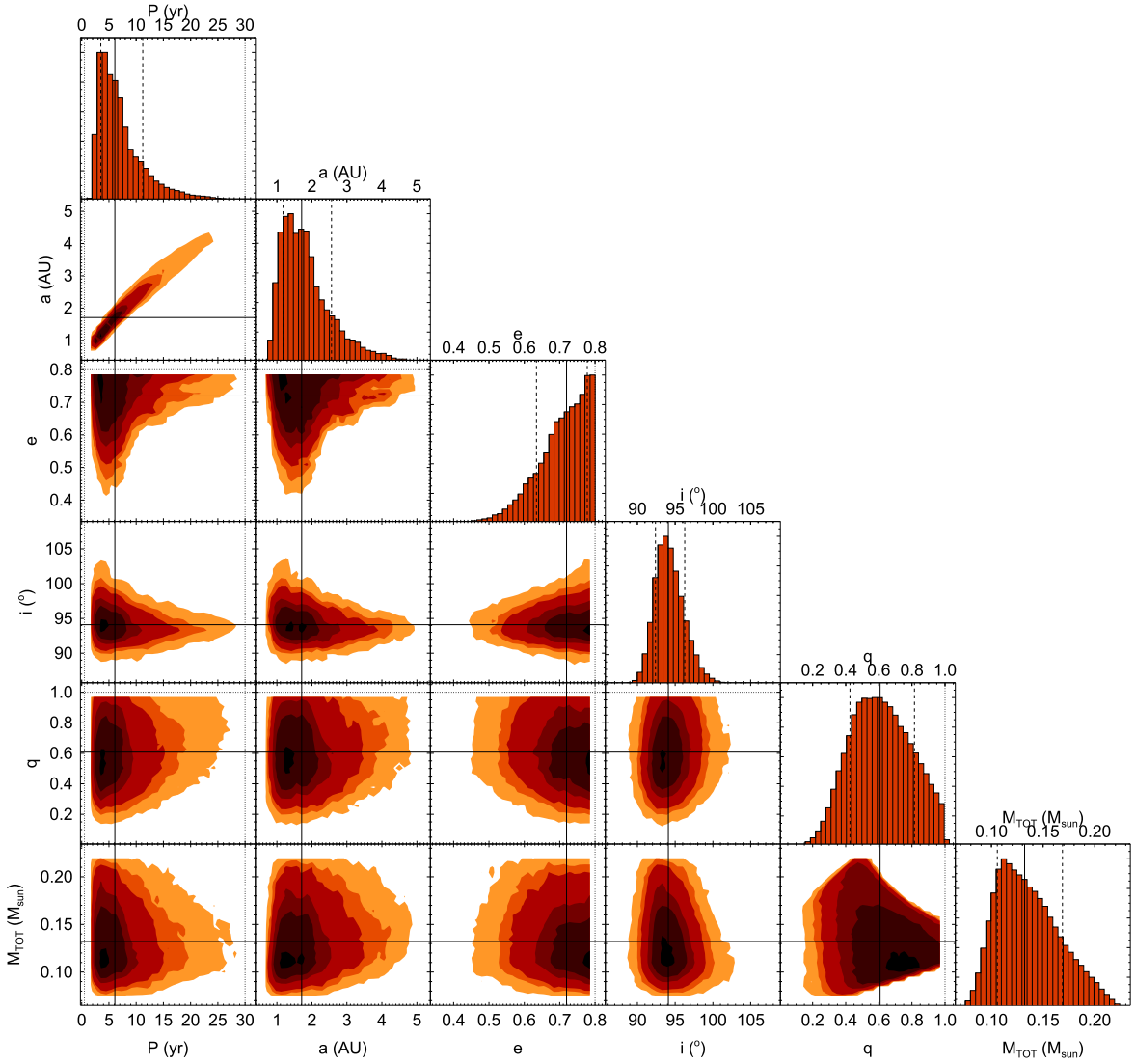

Figure 9. Parameter distributions and correlations (triangle plot) for period (P), semimajor axis (a), eccentricity (e), inclination (i), mass ratio (q) and total system mass ($M_{\rm tot}$) based on our MCMC orbital analysis for the NIRSPEC + NIRC2 data. The fits assume a weak constraint on eccentricity ($0 \leqslant e \leqslant 0.8$) and period (0.5 year $\leqslant P \leqslant$ 30 years). Contour plots show two-dimensional χ^2 distributions for parameter pairs, highlighting correlations. Normalized histograms at the ends of rows are marginalized over all other parameters. Median values are indicated by solid lines in all panels; 16% and 84% quantiles are indicated by dashed lines in the histograms. Imposed parameter limits for P and e are indicated by dotted lines.

ascending node ($\Omega = 82\overset{\circ}{.}7 \pm 2\overset{\circ}{.}1$) and the center of mass RV ($V_{\rm COM} = +87.4 \pm 0.8$ km s^{-1}). The tight constraints on i and Ω stem from the near-radial motion of the secondary between the two NIRC2 epochs. The position angle of the secondary changed by only $5^\circ \pm 2^\circ$ between these two observations but the secondary has moved 40% further away; this is possible only when the orbit is viewed very close to edge-on or $e \approx 1$. As discussed below, even with an eccentricity at the proscribed limits, the inclination remains close to 90°. Similarly, Ω is constrained by the orientation of the orbit on the sky. The tight constraint on $V_{\rm COM}$ arises from the small variance in observed RVs and consistency in the values measured in the earlier epochs. The NIRSPEC + NIRC2 and Hamilton + NIRC2 datasets yield nearly identical values for all three of these parameters.

Parameter distributions for P, e and q are more weakly constrained, and the latter two abut the imposed limits, emphasizing that we do not yet have sufficient coverage of the orbit of WISE J0720–0846AB to robustly determine them.

To gain some insight on how the quality of the fits vary as e changes, we performed additional MCMC chains on Hamilton + NIRC2 data using models with fixed $e = 0.2$, 0.4, 0.6 and 0.8. Figure 12 and Table 5 display the results of this experiment. We found that all parameters remain consistent with the unconstrained MCMC analysis, although q and M_2 values are modestly smaller for the $e = 0.2$. Parameter uncertainties are considerably larger for the $e = 0.8$ case, in part reflecting the lower χ^2 values of viable solutions. It is clear that the $e = 0.2$ and $e = 0.4$ models are poor representations of the RV data, with best-fit χ^2 values that are significantly worse and can be eliminated with >95% confidence as compared to the unconstrained model.[12] This analysis supports an eccentic orbit for WISE J0720–0846AB, but a firm constraint on its value should emerge with further monitoring.

[12] This confidence level was computed using the F-test probability distribution function, comparing the unconstrained best-fit model ($\chi^2 = 2.84$, 3 degrees of freedom) to the constrained models ($\chi^2 = 39.3$ and 25.1, 4 degrees of freedom).

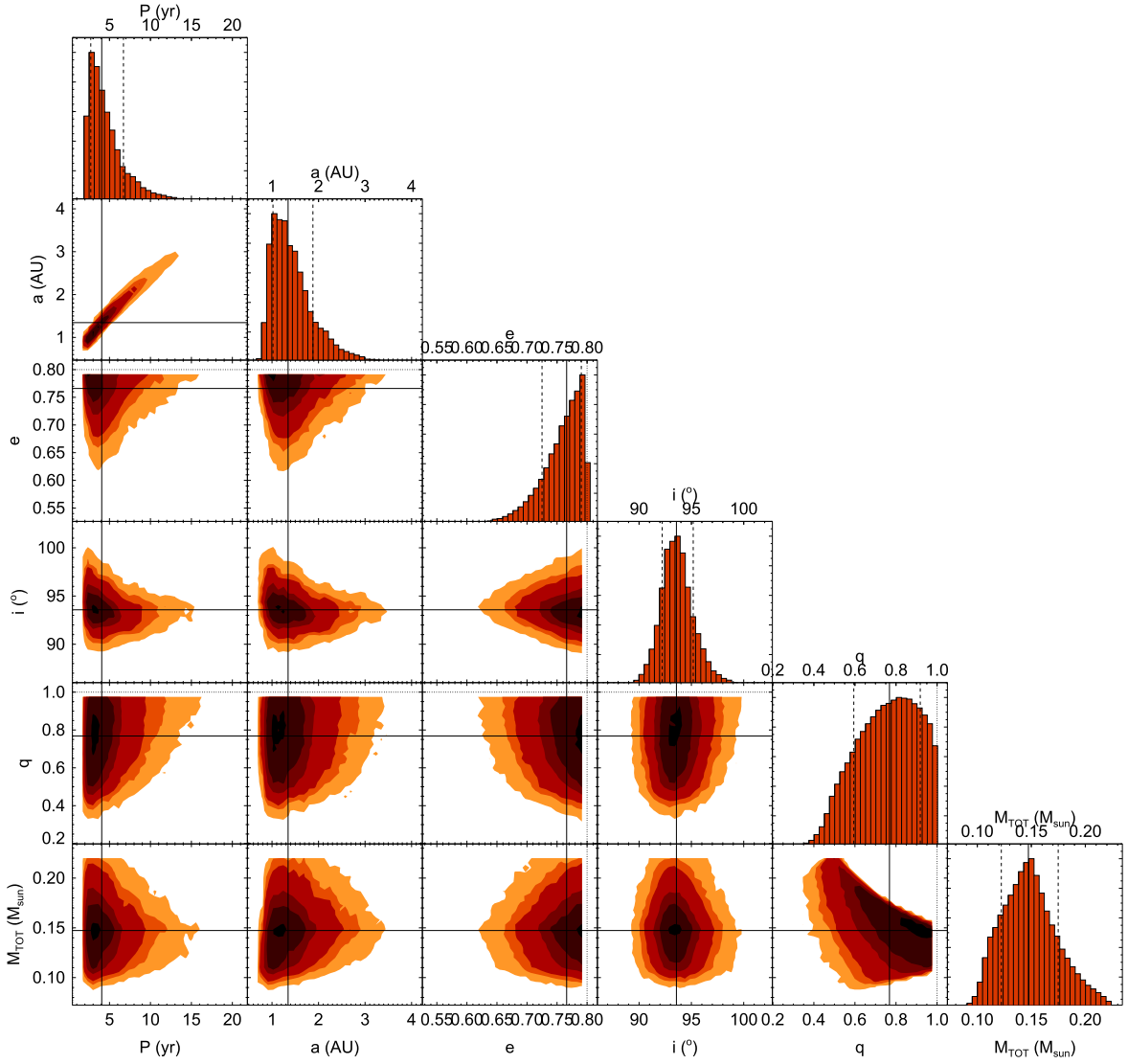

Figure 10. Same as Figure 9 for the Hamilton Spectrograph + NIRC2 data.

5. DISCUSSION

Our follow-up observations of WISE J0720–0846AB verify both the magnetic and binary nature of this nearby system, and provide first constraints on the physical properties of the components. While these first measurements of orbital motion do not robustly constrain system or component masses, they do constrain the orbital geometry, most notably inclination, which is within a few degrees of edge-on. The scale of this system is such that it is unlikely to eclipse; nevertheless, the orbit orientation allows us to make some constraints on the rotational properties of the primary. The orbital and primary rotational axes of main sequence binaries with close separations ($\lesssim$20 AU) are generally aligned (Weis 1974; Hale 1994). The only very low mass binary for which spin–orbit alignment has been tested, 2MASSW J0746425+200032AB, shows alignment between orbital and rotational axes of both components to within 5° (Harding et al. 2013). Assuming similar alignment of the rotational and orbital axes of WISE J0720–0846A and a radius of 0.1 $R_\odot$, our v sin i measurement implies a rotation period of 14.2 $\pm$ 0.7 hr. This value is remarkably close to the marginally indicated variability period from white light monitoring reported in B15, 14.00 $\pm$ 0.05 hr for a 1.3 $\pm$ 0.5% variability amplitude. The rotation period is somewhat slower than the mean for comparably classified sources (Irwin et al. 2011) and considerably slower than most highly variable L and T dwarfs (Radigan et al. 2014; Metchev et al. 2015). Its slow rotation rate and orientation may explain the weaker than average magnetic emission of WISE J0720–0846A, in both optical and radio bands, and its somewhat low flaring rate compared to other late M dwarfs. In addition, with a 1–2 AU semimajor axis, magnetospheric interaction between primary and secondary is unlikely to play a role in driving magnetic emission in either source (Schrijver 2009).

A more promising role for WISE J0720–0846AB is as a testbed for brown dwarf evolutionary models. As demonstrated by several studies (e.g., Liu et al. 2008, 2010; Konopacky et al. 2010; Dupuy et al. 2014), the inferred masses and atmospheric parameters of several very low mass binaries diverge to varying degrees from evolutionary model predictions. Limiting factors for such analyses include lack of knowlege of detailed spectra for individual components, inability to measure component masses, low quality distance determinations, and/or lack of independent age determinations.

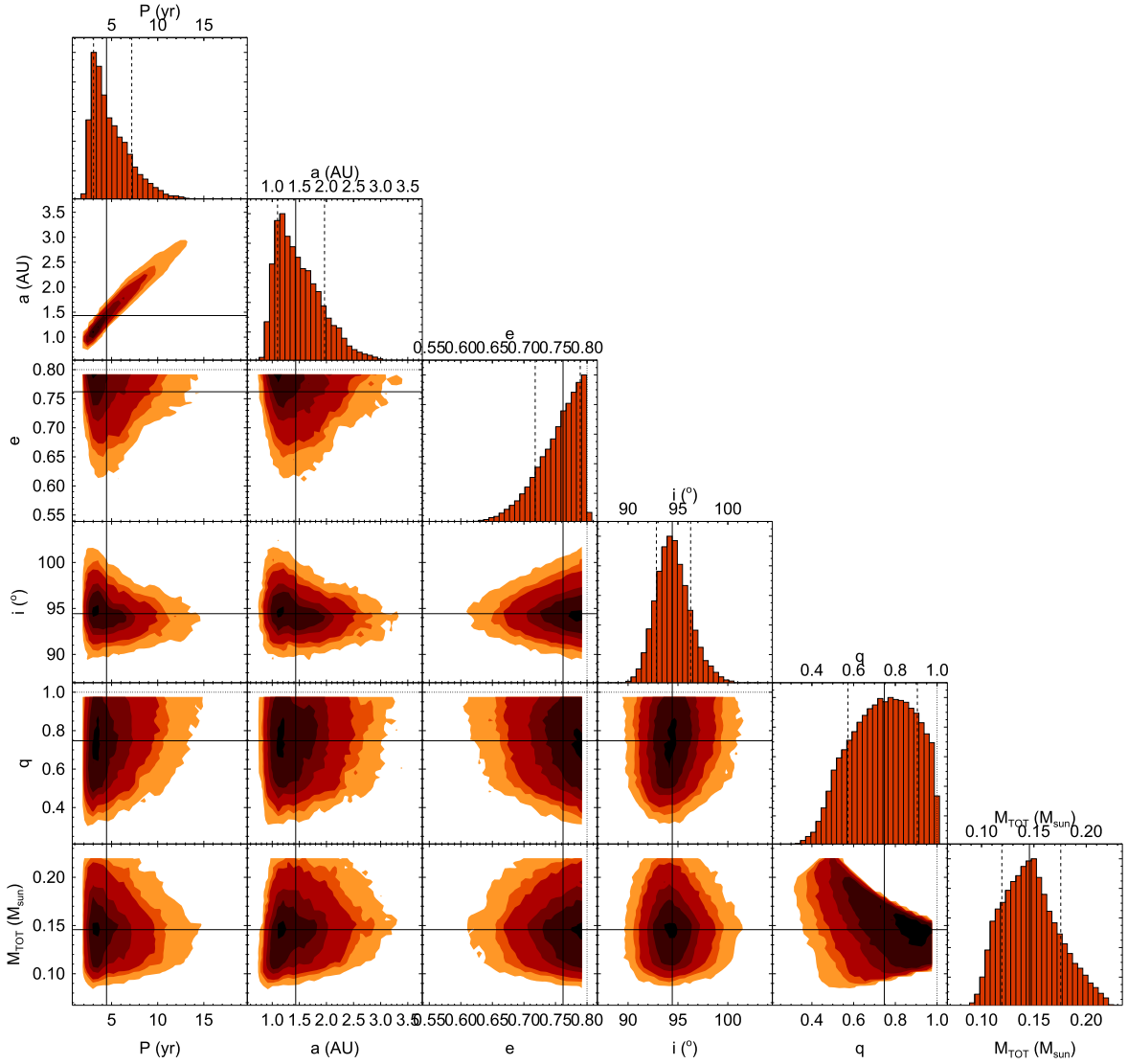

Figure 11. Same as Figure 9 for all RV and imaging data.

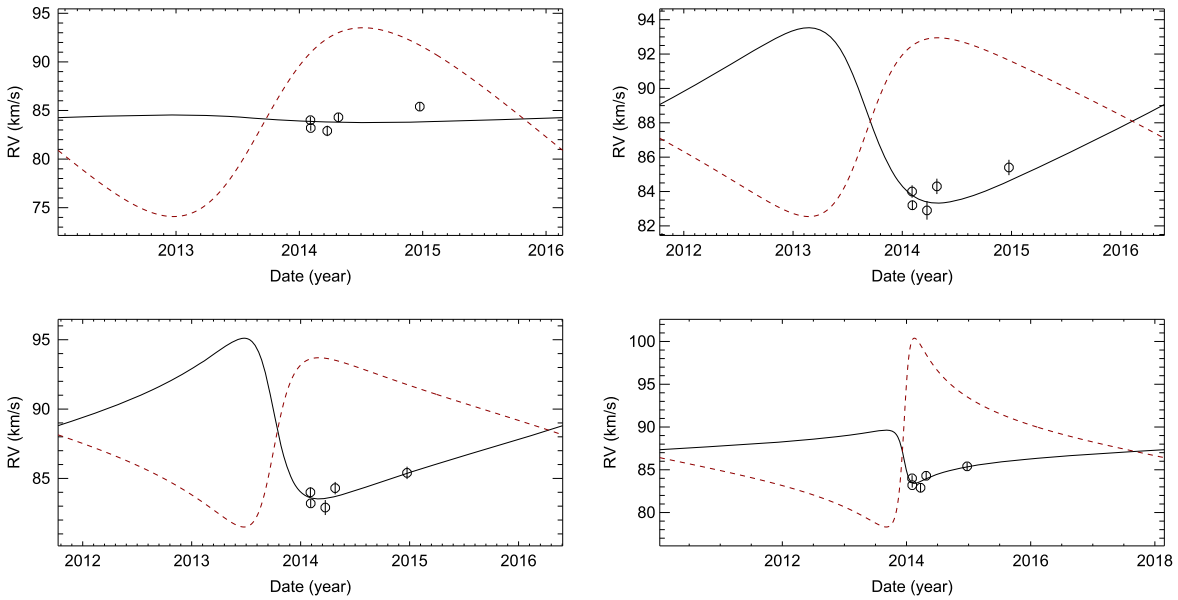

Figure 12. Predicted primary (black solid line) and secondary (red dashed line) radial velocities based on best-fit orbits with eccentricity fixed at 0.2 (upper left), 0.4 (upper right), 0.6 (lower left) and 0.8 (lower right), compared to NIRSPEC data. Compare to Figure 8.

Table 5
Parameters from Orbital Analysis of Hamilton + NIRC2 Data with Eccentricity Fixed

Parameter	$e = 0.2$	$e = 0.4$	$e = 0.6$	$e = 0.8$
Best χ^2	39.3	25.1	10.4	2.8
P[a] (year)	$4.4^{+0.8}_{-0.7}$	$4.3^{+1.0}_{-0.8}$	$4.2^{+1.2}_{-0.9}$	$3.8^{+3.0}_{-1.3}$
a (AU)	$1.40^{+0.18}_{-0.16}$	$1.38^{+0.23}_{-0.18}$	$1.4^{+0.3}_{-0.2}$	$1.3^{+0.6}_{-0.3}$
i (°)	$94.1^{+1.5}_{-1.3}$	$94.4^{+1.4}_{-1.3}$	$94.2^{+1.5}_{-1.3}$	$93.5^{+2.0}_{-1.6}$
q[a]	$0.69^{+0.19}_{-0.20}$	$0.80^{+0.14}_{-0.18}$	$0.82^{+0.13}_{-0.17}$	$0.73^{+0.16}_{-0.18}$
$V_{\rm COM}$ (km s^{-1})	$85.9^{+0.5}_{-0.6}$	$86.5^{+0.5}_{-0.5}$	$87.0^{+0.5}_{-0.5}$	$87.3^{+0.9}_{-0.9}$
$M_{\rm tot}$ ($M_\odot$)	$0.14^{+0.03}_{-0.03}$	$0.14^{+0.03}_{-0.02}$	$0.15^{+0.02}_{-0.02}$	$0.15^{+0.03}_{-0.03}$
M_1 ($M_\odot$)	$0.083^{+0.032}_{-0.018}$	$0.079^{+0.024}_{-0.014}$	$0.079^{+0.022}_{-0.013}$	$0.083^{+0.028}_{-0.017}$
M_2 ($M_\odot$)	$0.059^{+0.011}_{-0.014}$	$0.064^{+0.008}_{-0.011}$	$0.066^{+0.007}_{-0.010}$	$0.062^{+0.009}_{-0.011}$

Note.
[a] Parameter was constrained to a limited value range in MCMC analysis.

While the last factor may be challenging to overcome for WISE J0720–0846AB, the proximity and detection of reflex motion in both astrometric and radial coordinates allows the first three to be addressed, and we anticipate that this system will provide a high-quality test of models in the next 5–10 years.

Finally, we note that despite being able to detect reflex motion in the primary, the inferred close passage of WISE J0720–0846AB to the Sun deduced by Mamajek et al. (2015) on the basis of the system kinematics is not ruled out. The systemic motion estimated here is about 4 km s^{-1} larger than that assumed by these authors, so the impact parameter is roughly 5% smaller. The astrometric perturbation of the primary induced by the secondary, of order 100 mas, is sufficiently slow to play little role in modulating the parallax or proper motion of the system significantly given current measurement uncertainties. Improved monitoring of the systemic orbital motion will be needed to make a more precise estimate of the geometry and timescale of WISE J0720–0846AB's closest approach, and the corresponding perturbation it has made on our Oort cloud comet population.

The authors thank Randy Campbell, Heather Hershley, and Marc Kassis at Keck Observatory; and Pavl Zachary and Shawn Stone at Lick Observatory for their assistance with the observations. We thank our anonymous referee for her/his/their helpful comments, particularly on the MCMC analysis. C. M. acknowledges funding support from the National Science Foundation under award No. AST-1313428. The material is based upon work supported by the National Aeronautics and Space Administration under Grant No. NNX15AI75G. This research has made use of the SIMBAD database, operated at CDS, Strasbourg, France; NASA's Astrophysics Data System Bibliographic Services; the M, L, T, and Y dwarf compendium housed at DwarfArchives.org; and the SpeX Prism Libraries at http://www.browndwarfs.org/spexprism. Research at Lick Observatory is partially supported by a generous gift from Google. The authors recognize and acknowledge the very significant cultural role and reverence that the summit of Mauna Kea has always had within the indigenous Hawaiian community. We are most fortunate and grateful to have the opportunity to conduct observations from this mountain.

REFERENCES

Allard, F., Homeier, D., & Freytag, B. 2012, RSPTA, 370, 2765
Antonova, A., Hallinan, G., Doyle, J. G., et al. 2013, A&A, 549, A131
Basri, G., & Marcy, G. W. 1995, AJ, 109, 762
Berger, E. 2006, ApJ, 648, 629
Blake, C. H., Charbonneau, D., & White, R. J. 2010, ApJ, 723, 684
Burgasser, A. J. 2014, in Proc. 2013 Int. Workshop on Spectral Stellar Libraries, ASI Conf. Ser. Vol. 11, ed. H. P. Singh, P. Prugniel, & I. Vauglin, 7
Burgasser, A. J., Bardalez-Gagliuffi, D. C., & Gizis, J. E. 2011, AJ, 141, 70
Burgasser, A. J., Gillon, M., Melis, C., et al. 2015, AJ, 149, 104
Burgasser, A. J., Luk, C., Dhital, S., et al. 2012, ApJ, 757, 110
Burgasser, A. J., & McElwain, M. W. 2006, AJ, 131, 1007
Burgasser, A. J., McElwain, M. W., Kirkpatrick, J. D., et al. 2004, AJ, 127, 2856
Burgasser, A. J., & Putman, M. E. 2005, ApJ, 626, 486
Caffau, E., Ludwig, H.-G., Steffen, M., Freytag, B., & Bonifacio, P. 2011, SoPh, 268, 255
Dupuy, T. J., & Liu, M. C. 2011, ApJ, 733, 122
Dupuy, T. J., Liu, M. C., & Ireland, M. J. 2014, ApJ, 790, 133
Ford, E. B. 2005, AJ, 129, 1706
Gelman, A., & Rubin, D. B. 1992, StaSc, 7, 457
Gizis, J. E., Monet, D. G., Reid, I. N., et al. 2000, AJ, 120, 1085
Greisen, E. W. 2003, in Information Handling in Astronomy—Historical Vistas, Astrophysics and Space Science Library, Vol. 285, ed. A. Heck (Dordrecht: Kluwer), 109
Hale, A. 1994, AJ, 107, 306
Hallinan, G., Bourke, S., Lane, C., et al. 2007, ApJL, 663, L25
Harding, L. K., Hallinan, G., Konopacky, Q. M., et al. 2013, A&A, 554, A113
Hastings, W. K. 1970, Biometrika, 57, 97
Innes, R. T. A. 1907, Obs, 30, 310
Irwin, J., Berta, Z. K., Burke, C. J., et al. 2011, ApJ, 727, 56
Ivanov, V. D., Vaisanen, P., Kniazev, A. Y., et al. 2015, A&A, 574, A64
Kirkpatrick, J. D., Reid, I. N., Liebert, J., et al. 2000, AJ, 120, 447
Kirkpatrick, J. D., Schneider, A., Fajardo-Acosta, S., et al. 2014, ApJ, 783, 122
Konopacky, Q. M., Ghez, A. M., Barman, T. S., et al. 2010, ApJ, 711, 1087
Krishnamurthi, A., Leto, G., & Linsky, J. L. 1999, AJ, 118, 1369
Liu, M. C., Dupuy, T. J., & Ireland, M. J. 2008, ApJ, 689, 436
Liu, M. C., Dupuy, T. J., & Leggett, S. K. 2010, ApJ, 722, 311
Livingston, W., & Wallace, L. 1991, An atlas of the solar spectrum in the infrared from 1850 to 9000 cm-1 (1.1 to 5.4 micrometer) (Tucson, AZ: National Solar Observatory)
Mamajek, E. E., Barenfeld, S. A., Ivanov, V. D., et al. 2015, ApJL, 800, L17
McLean, I. S., Graham, J. R., Becklin, E. E., et al. 2000, Proc. SPIE, 4008, 1048
McLean, M., Berger, E., & Reiners, A. 2012, ApJ, 746, 23
Metchev, S. A., Heinze, A., Apai, D., et al. 2015, ApJ, 799, 154
Metropolis, N., Rosenbluth, A. W., Rosenbluth, M. N., Teller, A. H., & Teller, E. 1953, JChPh, 21, 1087
Osten, R. A., & Wolk, S. J. 2009, ApJ, 691, 1128
Radigan, J., Lafrenière, D., Jayawardhana, R., & Artigau, E. 2014, ApJ, 793, 75
Reid, I. N., Kirkpatrick, J. D., Gizis, J. E., & Liebert, J. 1999, ApJL, 527, L105
Schmidt, S. J., Hawley, S. L., West, A. A., et al. 2014, arXiv:1410.0014
Scholz, R.-D. 2014, A&A, 561, A113
Schrijver, C. J. 2009, ApJL, 699, L148
Simons, D. A., & Tokunaga, A. 2002, PASP, 114, 169
Stelzer, B., Micela, G., Flaccomio, E., Neuhäuser, R., & Jayawardhana, R. 2006, A&A, 448, 293
Stephens, D. C., Leggett, S. K., Cushing, M. C., et al. 2009, ApJ, 702, 154
Tokunaga, A. T., Simons, D. A., & Vacca, W. D. 2002, PASP, 114, 180
van Dam, M. A., Bouchez, A. H., Le Mignant, D., et al. 2006, PASP, 118, 310
van den Bos, W. H. 1927, BAN, 3, 261
Vogt, S. S. 1987, PASP, 99, 1214
Weis, E. W. 1974, ApJ, 190, 331
West, A. A., Hawley, S. L., Walkowicz, L. M., et al. 2004, AJ, 128, 426
Williams, P. K. G., & Berger, E. 2015, arXiv:1502.06610
Williams, P. K. G., Berger, E., & Zauderer, B. A. 2013, ApJL, 767, L30
Wizinowich, P. L., Le Mignant, D., Bouchez, A. H., et al. 2006, PASP, 118, 297
Wright, E. L., Eisenhardt, P. R. M., Mainzer, A. K., et al. 2010, AJ, 140, 1868